ELSEVIER

International Journal of Mass Spectrometry 222 (2003) 155–174

International Journal of Mass Spectrometry

www.elsevier.com/locate/ijms

Modeling the ion density distribution in collisional cooling RF multipole ion guides

Aleksey V. Tolmachev, Harold R. Udseth, Richard D. Smith*

Environmental Molecular Science Laboratory, MS K8-98, Pacific Northwest National Laboratory, P.O. Box 999, Richland, WA 99352, USA

Received 22 April 2002; accepted 6 August 2002

Abstract

Collisional cooling radio frequency (RF) multipoles are widely used in mass spectrometry, as ion guides and two-dimensional ion traps. Understanding the behavior of ions in these devices is important in choosing a multipole configuration and optimizing its performance. We have developed a computer model based on ion trajectory calculations in the RF multipole electric field, taking into account ion–ion and ion–neutral interactions. The two-dimensional model for idealized infinite RF multipoles gives an accurate description of the ion density distribution. We consider first a basic case of a single *m*/*z* ion cloud in the two-dimensional RF quadrupole after equilibrium is reached. Approximate theoretical relationships for the ion cloud configuration in the two-dimensional ion trap are tested based on the simulation results. Next we consider the case of an ion cloud consisting of several different *m*/*z* ion species. The ion relaxation dynamics and the process of establishing the stratified ion density distribution are observed. Simulations reveal that the ion kinetic energy relaxation dynamics are dependent on the ion population and bath gas pressure. The equilibrium distribution agrees well with the ion stratification theory, as demonstrated by simulations for RF quadrupole and octopole two-dimensional ion traps. (Int J Mass Spectrom 222 (2003) 155–174)

Keywords: Ion cooling; Mass range; Space charge; Computer modeling; Simulation

1. Introduction

Collisional cooling radio frequency (RF) multipole ion guides are used in mass spectrometry to transmit ions from an intermediate pressure region of an ion source (e.g., electrospray, or other ion source implementing differential pumping stages) into a higher vacuum region of a mass analyzer [1–3]. The effective potential formed by an inhomogeneous RF field [4] confines ions radially, while collisions with the buffer gas molecules lead to dissipation of initial ion kinetic energy, a process referred to as collisional cooling [1]. Collisionally cooled ions acquire reduced amplitudes of radial oscillations in the effective potential well and occupy a region close to the ion guide axis. The reduced ion kinetic energy spread provides improved ion focusing into the next region of an instrument. Another, rapidly developing application of the collisional cooling RF multipoles is for accumulation of ions, e.g., prior to transfer to the analyzer trap in FT ICR or other non-continuous mass analyzers, to improve sensitivity and dynamic range [5–17].

To determine optimal parameters for a collisional RF multipole, operated as an ion guide or trap, it

* Corresponding author. E-mail: rd_smith@pnl.gov

1387-3806/02/$ – see front matter
PII S1387-3806(02)00960-0

is necessary to understand the ion dynamics in the device. The ion motion is influenced by the fast changing RF field, ion–neutral collisions and ion–ion (space charge) interactions. Theoretical treatments of the radial ion density distribution in the collisional RF multipoles have been given in Refs. [18–20], and computer simulations of the collisional cooling have been reported in Refs. [1–3,21]. Similar approaches have been applied for computer modeling of ion motion in three-dimensional ion traps [22–25]. Most of the models are single-ion simulations, neglecting the space charge interaction of ions. More elaborate simulations taking into account the space charge interaction and using hard sphere models for ion–molecule collisions have been developed for behavior in ICR cells [26,27]. The collective oscillations of an ion cloud in three-dimensional traps have been considered [28].

In this work we report the computer simulation results for the radial ion density distribution for infinitely long RF multipoles, taking into account space charge and hard sphere ion–molecule interactions. Simulations were performed for a wide range of pressures and linear ion densities, and results were compared to theoretical relationships. We also considered a particularly relevant situation of an ion cloud consisting of several m/z species. A simplified low-ion energy model suggests ion density distributions consisting of cylindrical layers, each of them having a specific m/z, with higher m/z occupying larger radii [29,30]. This expectation has been examined using direct simulations, and conditions for establishing such m/z-stratified distributions are derived.

2. Methods

The simulation scheme used for this study is similar to approaches in Refs. [21–27]. A hard sphere elastic collision model is used to describe the ion–neutral interactions. During the time between collisions the vacuum equation of motion is used to calculate ion trajectories:

$$\frac{\mathrm{d}\boldsymbol{u}}{\mathrm{d}t} = \frac{q}{m}(\boldsymbol{E}_{\mathrm{DC}} + \boldsymbol{E}_{\mathrm{RF}} + \boldsymbol{E}_{\mathrm{SC}}) \quad (1)$$

where $\boldsymbol{u}$, q, and m are respectively the ion's velocity, charge and mass; the electric field, driving the ion motion, is calculated as a sum of the DC field $\boldsymbol{E}_{\mathrm{DC}}$, the RF field $\boldsymbol{E}_{\mathrm{RF}}$, and the space charge field $\boldsymbol{E}_{\mathrm{SC}}$. The bold variables $\boldsymbol{u}$, $\boldsymbol{E}_{\mathrm{DC}}$, $\boldsymbol{E}_{\mathrm{RF}}$, and $\boldsymbol{E}_{\mathrm{SC}}$ designate three-dimensional vectors; all of them are functions of the x, y, and z coordinates and all except $\boldsymbol{E}_{\mathrm{DC}}$ are time dependent. Eq. (1) is integrated numerically, using a standard second order Runge–Kutta algorithm [31].

A simulation run is organized as follows. At $t = 0$ an initial configuration of the ion cloud is created by generating coordinates of a certain number of ions, N_{ions}, so as to fill randomly the inner volume of the multipole. Then the ion motion of the whole ensemble is simulated; the position of each ion is updated every time step dt, taking into account the Coulombic interaction with other ions. The evolution of the ion cloud is followed up until an equilibrium state is reached. After the equilibrium configuration is established the simulation continues over a time interval needed to collect statistics on the ion density distribution.

We have reported the initial results in Ref. [29] that included both three- and two-dimensional simulations of the external accumulation multipoles. The three-dimensional simulations were necessary to evaluate the dynamics of ion trapping, relaxation, and extraction, where the inlet and exit orifice configurations are of importance. Under the three-dimensional approach the potential array relaxation technique, similar to one implemented in the SIMION program [32], is used to compute three-dimensional configuration of the $\boldsymbol{E}_{\mathrm{DC}}$ and $\boldsymbol{E}_{\mathrm{RF}}$ fields of the multipole. The space charge interaction was computed as a sum of Coulomb fields acting on each ion from all other ions. The simulation time for such algorithm is proportional to the number of particles N_{ions} squared, and the practically accessible number was $N_{\mathrm{ions}} \sim 1000$. To simulate ion densities of practical interest, each particle was considered as a group, N_{group}, of ions when computing the space charge field (the so called super-ion approximation).

The three-dimensional simulations have shown that upon completion of the collisional relaxation the ion density per unit length inside a multipole is practically constant and is not sensitive to the three-dimensional

fringing fields [29]. This behavior was also expected from the approximate analytical treatment in Ref. [20]. Thus a more accurate model has been implemented, that assumes an infinite, two-dimensional multipole. The model disregards the ion cloud behavior at the multipole ends, and concentrates on the ion density distribution in the inner axial region. The DC field $\boldsymbol{E}_{\mathrm{DC}}$ is neglected under this two-dimensional model, and the RF field is calculated using analytical relationships [33]. The space charge field is calculated assuming that each simulated particle represents an infinite line of charges, so instead of the Coulombic $1/r^2$ interaction, the $1/r$ dependence is used for $\boldsymbol{E}_{\mathrm{SC}}$ computation. The two-dimensional approach is more efficient than the three-dimensional one and permits accurate calculation of the radial ion density distribution. All results presented here have been obtained using this two-dimensional approach.

To verify the method stability and to estimate computational errors due to the coarseness of the time step and the super-ion approximation, the equilibrium ion distribution was computed for different time steps and different N_{group} coefficients. Stable and reproducible results were obtained for time steps of $\sim 10^{-2}$ of one RF period and for N_{group} coefficients sufficiently small so that the number of super-ions per characteristic ion cloud dimension is $\gg 1$. Typical time for a simulation run ranges from $\sim$1 h to several days using a 600 MHz Pentium III PC computer. The following additional tests of the computational accuracy were used. The ion trajectory integration procedure was verified on the basis of the low-mass cut-off, or the onset of unstable ion motion in the RF only quadrupole, for a q-parameter exceeding the limit [31]:

$$q_m = \frac{4qV_{\mathrm{RF}}}{m\omega^2\rho^2} \geq 0.908 \qquad (2)$$

We use the notation q_m for the q-parameter, to distinguish it from the ion charge q; V_{RF} is the RF voltage amplitude (i.e., 0-peak and pole to ground voltage), $\omega = 2\pi f$ is the angular frequency, corresponding to the RF, f, and ρ is the inscribed radius of the quadrupole. The model demonstrated exact coincidence with the theoretical instability onset for the time steps $\mathrm{d}t \lesssim 10^{-2}/f$ (the tests were performed under conditions of a negligible space charge). The multiparticle approach for the space charge field computation was tested by comparison of the radial ion density distribution with the theoretical distribution derived for the low-ion energy case. Good agreement was achieved for the two-dimensional model, as will be discussed in the following section. The three-dimensional model produced a rough approximation of the radial ion density for practically useful values of the N_{group} and $\mathrm{d}t$ parameters, however, characteristic dimensions of the ion cloud still can be calculated under this model with relative accuracy $\sim 10^{-2}$. When the number of simulated particles was increased (and N_{group} proportionally decreased), the computed radial distribution converged to one obtained from two-dimensional model, but it took considerably longer computation times.

An important parameter related to the accuracy of the super-ion space charge simulations is the dimension of an ion cloud representing the super-ion, R_{group}. If this parameter is set to 0, the Coulombic interaction of two closely positioned super-ions results in overestimating of the Coulombic field. For a long simulation, using $t \gtrsim 10^6$ time steps ($t \gtrsim 10$ ms) this may result in increased ion kinetic energy, due to accumulation of computational errors. This artifact is pronounced for low pressures, $p < 10^{-4}$ Torr, where collisional relaxation does not mask the energy increase. The problem may be solved by setting a finite super-ion radius R_{group}, so that for a short distance $d < R_{\mathrm{group}}$ the force between two super-ions E_{ij} is calculated under the assumption that the charge is distibuted uniformly inside each super-ion. Thus $E_{ij} \propto d$ for $d < R_{\mathrm{group}}$, so that close position of two super-ions does not lead to an overestimation of their interaction. The value R_{group} is calculated from a condition that the volume of all super-ions must approximately cover the total ion cloud volume, thus $R_{\mathrm{group}} \propto N_{\mathrm{ions}}^{-3}$ for the three-dimensional model and $R_{\mathrm{group}} \propto N_{\mathrm{ions}}^{-2}$ for the two-dimensional model. We see that the spatial resolution of the space charge simulation approach, limited by the R_{group} value, may be improved by using a larger number of super-ions N_{ions}, and the two-dimensional

model allows one to reach a better resolution for a given N_{ions} number. In the simulations reported in the following description, we have used $R_{group} \sim 10^{-2}\ \rho$ for the two-dimensional model.

A possible alternative to the super-ion approach is the particle-in-cell method (PIC) (see Refs. [26,27] and references therein). Under the PIC approach the space charge electric field is calculated not by summing the N_{ions}^2 Coulomb fields, but rather from a computational grid on which Poisson's equation is solved numerically for the potential at each time step. The PIC's computational time T_{comp} is proportional to N_{ions}, not N_{ions}^2, and the number of simulated particles may be increased up to $>10^5$. However, it does not necessarily result in improved spatial resolution of a simulated ion cloud, because the resolution is now defined by the grid step size D_{grid}. The simulation time T_{comp} becomes proportional to a size of computational mesh, thus $T_{comp} \propto D_{grid}^2$ for two-dimensional model and $T_{comp} \propto D_{grid}^3$ for three-dimensional model. For example the computational mesh used in the two-dimensional simulations [26] had ~100 mesh steps in one-dimensional, which is roughly equivalent to the resolution of $R_{group} \sim 10^{-2}\ \rho$ estimated earlier for the super-ion approach used here. A distinctive feature of a system under consideration here is that very fast RF oscillations of ions define a small time step, <10 ns for $f > 1$ MHz, and the total time interval needed to be simulated is >0.1 s, so the total number of time steps may be $>10^7$. In the case of the PIC algorithm it means that the Poisson's equation must be solved numerically 10^7 times during a single simulation. This would result in impractically long computation time, even for a very rough computation mesh. The super-ion approach used here has been realized on a regular desktop PC computer using Windows 98 operating system, and may be run in background mode on several PCs, to look at several different configurations at the same time.

The ion–neutral interaction model used in the simulations is based on the classical hard spheres collisions approach. For the case of relatively large biomolecules of interest it has been shown [34–36] that the hard-core cross-section dominates the ion-dipole cross-section. The so-called diffuse scattering model produced a better description of the ion–neutral collisions, although the specular elastic scattering has not produced much different results in terms of the cross-section of collisions [35]. We use here the classical elastic hard sphere model; the diffuse scattering, or inelastic collisions, may also be incorporated, but are not considered here.

The hard sphere collision algorithm implemented in our model is based on the Monte–Carlo simulation of collisions of a hard sphere representing an ion with hard spheres representing the bath gas molecules. The velocity of the bath gas molecules v is assumed to be distributed according to the Maxwell–Boltzmann distribution:

$$f_m(v) = 4\pi v^2 (\pi v_{kT}^2)^{(-3/2)} \exp\left(-\frac{v^2}{v_{kT}^2}\right);$$
$$v_{kT}^2 = \frac{2kT}{m_g} \tag{3}$$

where k is the Boltzmann constant, T and m_g are the bath gas temperature and molecular mass. The frequency of collisions is calculated from the relative velocity v_{rel} as $z = n\sigma v_{rel}$, where n is the number density of the bath gas molecules, σ is the collision cross-section. To find an overall probability of collisions taking into account all possible magnitudes and directions of neutrals, it is convenient to consider first a simplified velocity distribution, in which all neutrals have the same velocity v, uniformly distributed in all possible directions. This so-called mono-velocity model has been described in Ref. [18]. For the ion velocity u we have the relative velocity $v_{rel} = (v^2 + u^2 - 2uv\cos\theta)^{1/2}$, where θ is the angle between the two velocity vectors. Averaging over all possible directions θ gives an average relative velocity for the mono-velocity model v_a:

$$v_a(u, v) = \int_0^\pi \sqrt{v^2 + u^2 - 2uv\cos\theta}\, d\Omega$$
$$= \begin{cases} u + \dfrac{v^2}{3u}, & \text{for } v < u \\ v + \dfrac{u^2}{3v}, & \text{for } v \geq u \end{cases} \tag{4}$$

where $d\Omega = 1/2 \sin\theta d\theta$ is the element of the solid angle. Now we can take into account the Maxwell–Boltzmann distribution, arriving at the frequency of collisions as a function of the ion velocity:

$$z(u) = n\sigma v_m(u); \quad v_m(u) = \int_0^\infty f_m(v) v_a(u, v) dv \tag{5}$$

Here $v_m(u)$ is the relative velocity of collisions averaged over the Maxwell–Boltzmann distribution. The function $z(u)$ was calculated and stored in a table for a range of all possible ion velocities u. Note that for ion velocities much higher than the thermal velocity, $u \gg v_{kT}$, the Eq. (4) gives $v_a \sim u$ and $z(u) \sim n\sigma u$. Thus, practically the $z(u)$ table needs to be calculated up to $u \sim 10 v_{kT}$. Having the $z(u)$ tabulated it is easy to define the probability of collisions on each time step dt: $P_c = z(u)dt$. It was assumed here that the time step dt is small enough so that $P_c \ll 1$. At each time step the program generates a random number R, uniform between 0 and 1; if $P_c > R$ then the collision event occurs.

This approach for the collision probability computation is different from approaches used elsewhere, where the relative velocity is computed on the basis of the neutral velocity taken randomly from the Maxwell–Boltzmann distribution. The advantage of our approach is that the collision probability P_c for each time step corresponds to the accurate theoretical value, whereas the alternative approach gives an accurate result only on average, after statistically large number of time steps, when all possible values from the two-dimensional (v,θ) space are sampled. Our approach also can be more efficient in terms of computation time, because it is not necessary to calculate the relative velocity $v_{rel} = (v^2 + u^2 - 2uv\cos\theta)^{1/2}$ at each time step.

The collision is simulated by giving a random direction to the ion velocity vector in the center-of-mass frame, as described in Refs. [3,21,26]. To define the center-of-mass velocity of an ion all three components of the neutral's velocity v_x, v_y, and v_z, are needed. We obtain the components using a randomly generated absolute velocity v, the scattering angle θ defined earlier, and the azimuthal angle φ. Here we take into account that the probability of collisions is not the same for each (v,θ) pair. Two random numbers, uniform from 0 to 1, are generated, to define v and θ values, according to the Monte–Carlo method of a projection of a variable x, having distribution $f_x(x)$, to a random number $R(x)$, uniform from 0 to 1 [37]:

$$R(x) = \int_0^x f_x(\xi) d\xi \tag{6}$$

Consider first the distribution f_v of the neutral's velocity v. Using the same procedure as for deriving the average relative velocity $v_m(u)$ (5), we can obtain the following distribution:

$$f_v(u, v) = f_m(v) \frac{v_a(u, v)}{v_m(u)} \tag{7}$$

The distribution for the θ angle follows from the frequency of collisions as a function of θ. After the neutral's velocity v is generated we can use the monovelocity relationships (4) to define the θ distribution as:

$$f_\theta(\theta) = \frac{\sin\theta}{2v_a(u, v)} \sqrt{v^2 + u^2 - 2uv\cos\theta} \tag{8}$$

Thus, applying the Monte–Carlo algorithm (6) first for f_v and then for f_θ distribution, we can generate the (v,θ) pair for a collision. The azimuthal angle φ is randomly distributed from 0 to 2π. After all three parameters are generated the collision is defined in the ion's coordinate system. Then the transition is made to the lab frame. All three components of the ion velocity are calculated for the center-of-mass system (CMS). The ion velocity after collision is calculated as the velocity before collision in the CMS, deflected at a random angle, the same manner as in other implementations of the hard sphere algorithm [3,21,26]. This relatively complicated algorithm can be still quite efficient because the collision event typically occurs after a large number of time steps. To speed up the computation we have used pre-calculated tables for $v_a(u,v)$ and $f_m(v)$ functions.

Several tests have been made to verify the hard sphere collisions algorithm, to make sure that both the principal part and the coding are correct. In the case

when no electric field is applied the distribution of the velocity of ion u approaches the Maxwell–Boltzmann distribution, same as (3), but with molecular mass m_g replaced by the ion mass m. In accordance with the theory [18], the collisional relaxation from initial ion velocity to the thermal equilibrium state proceeds exponentially with characteristic time:

$$\tau = \frac{3(m+m_g)}{4m_g n\sigma u_{kT}}; \quad u_{kT} = \sqrt{\frac{8kT}{\pi m_r}} \tag{9}$$

where m_r is the reduced mass. Another test is based on the collisional relaxation path, defined as the length of a linear path of the ion before its initial velocity is dissipated. The process was simulated using the hard sphere model described here, and showed a close agreement with a dependence estimated analytically, as reported in Ref. [18]. The random walk of an ion after collisional relaxation may be described by a diffusion coefficient D. The mean-squared displacement $\langle l^2 \rangle$ of an ion over a time interval t, corresponding to a statistically large number of collisions, was calculated and compared with the theoretical relation: $\langle l^2 \rangle = 6Dt$, and a close agreement was obtained. Finally, the test of the drift ion motion has been done, under which an average ion drift velocity, u_{drift}, was calculated. An electric field E was chosen so that the drift velocity is small compared to the thermal velocity of the bath gas molecules, $u_{\text{drift}} \ll v_{kT}$. The result agreed well with the theoretical relation $u_{\text{drift}} = K_E E$. The mobility coefficient K_E and the diffusion coefficient values D were calculated according to the classical theory of mobility [38]. Here it is convenient to express the two constants through the velocity relaxation time τ [18]:

$$K_E = \frac{q}{m}\tau; \quad D = \frac{kT}{q}K_E = \frac{kT}{m}\tau \tag{10}$$

Thus, all these tests of the new hard sphere collision algorithm have confirmed that it provides an accurate description of this classical model. The collisional cooling dynamics simulations reported elsewhere use simplifying assumptions. The problem is complicated first because the drag coefficient approach must be applied when the ion energy is ~10 eV [35,36], and second, the non-equilibrium statistical description has to be used on the final stage of the ion relaxation, when the ion–neutral interactions have mainly a random thermal origin. Additional complication arises due to a strong non-uniform RF electric field that causes the kinetic energy of ions to change from 0 up to ~10 eV each RF period. To adequately describe this complex system one needs a reliable and accurate model for the ion–neutral interactions. Here we have chosen the classical hard sphere model that is capable of describing all the processes of the ion collisional relaxation, using no additional assumptions.

3. Results and discussion

The ion density distribution was found to be cylindrically symmetric up to the statistical uncertainty of computations. Thus, the results can be presented as the ion number density (i.e., the number of particles per unit volume) vs. radius, $n(r)$. Fig. 1 shows the equilibrium ion density distribution in the RF collisional quadrupole, for three different linear charge densities. The RF parameters are typical for an external accumulation setup: $V_{\text{RF}} = 60$ V (0 to peak), frequency 600 kHz. The inscribed radius of the quadrupole is $\rho = 4$ mm. Singly charged ions $m = 1000$ are considered, corresponding to a q-parameter $q_m = 0.10$ Eq. (2). The bath gas parameters used are: molecular mass $m_g = 29$, pressure of 10 mTorr, and cross-section of the ion–molecule collisions $\sigma = 200$ A^2.

Fig. 1 shows the ion number density radial profiles for three different linear charge densities. To understand this behavior, we can use simple relationships for the basic ion density parameters, obtained previously. The simplest approach is based on the assumption of zero random energy, or zero temperature of ions [19,20]. From the balance of the space charge force and the effective RF focusing force one can obtain the following expression for the maximum possible ion number density in the RF quadrupole:

$$n_0 = q_m \varepsilon_0 \frac{V_{\text{RF}}}{q\rho^2} \tag{11}$$

Thus the ion number density is a constant that is independent of the radial coordinate and is defined

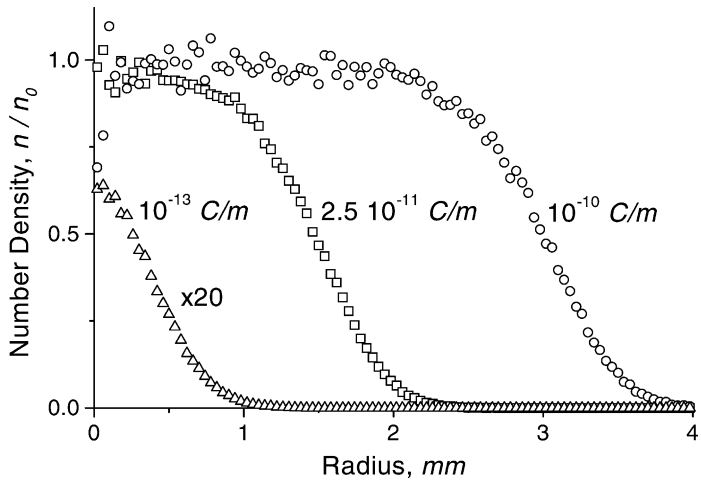

Fig. 1. Ion number density distribution simulated for RF collisional quadrupole, for three linear ion density values: 1×10^{-13} C/m ($R_q = 0.1$ mm), 2.5×10^{-11} C/m ($R_q = 1.5$ mm), and 1×10^{-10} C/m ($R_q = 3$ mm). Estimated thermal radius $R_{kT} = 0.5$ mm. Ions are singly charged ($m = 1000$). RF quadrupole parameters are as follows: $\rho = 4$ mm, $V_{RF} = 60$ V, frequency 600 kHz, $q_m = 0.10$, and pressure 10 mTorr.

by the RF quadrupole parameters. Under the zero-temperature approximation the number density of ions is always equal to the maximum number density n_0, no matter how many ions are stored. The linear charge density Q_l may be expressed via the number density as follows:

$$Q_l = \pi R_q^2 q n_0 \tag{12}$$

When the ion cloud radius R_q reaches the inscribed quadrupole radius ρ, the linear charge density reaches the maximum possible charge capacity:

$$Q_{max} = \pi \rho^2 q n_0 = \pi q_m \varepsilon_0 V_{RF} \tag{13}$$

This relationship gives an upper estimate of the RF quadrupole charge capacity [20]. For linear charge densities lower than Q_{max} the ions form a cylinder with a constant number density n_0 (11), and the radial dimension

$$R_q = \rho \sqrt{\frac{Q_l}{\pi \varepsilon_0 q_m V_{RF}}} \tag{14}$$

This simplified picture roughly agrees with the simulation results in Fig. 1. The number density, plotted in n_0 units, tends to 1 for the two higher linear charge densities, confirming the estimation given by Eq. (11).

The radial size approximately agrees with Eq. (14) ($R_q = 1.5$ mm for $Q_l = 2.5 \times 10^{-11}$ C/m and $R_q = 3.0$ mm for $Q_l = 1 \times 10^{-10}$ C/m). However, unlike the zero-temperature distribution, the simulated distribution posses a wing, extending to radii $>R_q$. This "diffusion spread" has been considered in [20]:

$$\Delta r \approx \sqrt{\frac{16 \varepsilon_0 kT}{q^2 n_0}} \tag{15}$$

For the values of parameters used in Fig. 1 one can estimate the diffusion spread using Eq. (15), as $\Delta r \approx 1$ mm. This approximately corresponds to the diffusion spread size shown in Fig. 1. We conclude that the relationship (15) gives a reasonably good estimation for the radial spread of the wing of the ion density distribution. However, it must be emphasized that under certain conditions the random component of the ion kinetic energy can be significantly higher than the thermal energy kT. This can be expected when ions are "heated" by an intense RF excitation, either by increased RF fields at large radial positions, or when the q_m parameter approaches the low-mass cut-off, $q_m \sim 0.9$. Simulations for the increased ion energy for the latter case have been reported in [39]. Under such

conditions the value given by Eq. (15) underestimates the actual radial spread. Alternatively, Eq. (15) may produce overestimation for low-pressure conditions considered later.

The ion density distribution corresponding to the low linear ion density, $Q_l = 10^{-13}$ C/m, in Fig. 1, does not reach the maximum number density n_0. In this case the zero-temperature approximation should be replaced by an approach that assumes a negligible space charge and a random ion kinetic energy at the thermal level [18]. In this case the equilibrium ion density distribution takes the form of the Boltzmann distribution for a thermal particle moving in the potential well formed by the effective potential. For the case of RF quadrupole this corresponds to the Gaussian distribution [18–20]:

$$n(r) \propto \exp\left(-\frac{r^2}{R_{kT}^2}\right) \tag{16}$$

The average-squared radial position R_{kT} is as follows [18]:

$$R_{kT} = 2\rho\sqrt{\frac{kT}{q_m q V_{RF}}} \tag{17}$$

For the conditions of Fig. 1, $R_{kT} = 0.5$ mm (it can be seen that $R_{kT} = \Delta r/2$ by definition). We see that the ion density distribution for the lowest linear charge density roughly agrees with the thermal approximation. One can predict the transition to the thermal distribution, by comparing the estimated values R_q (14) and R_{kT} (17). Here we have $R_q = 0.1$ mm $\ll R_{kT}$, meaning that the thermal spread defines the shape of the distribution.

Summarizing the results for Fig. 1 we conclude that the simple approximate relationships allow one to predict the main characteristics of the ion density distribution. The maximum charge capacity estimated using the zero-temperature approximation, Eq. (13), seems to be reasonably good. For the conditions of Fig. 1, Eq. (13) gives $Q_{max} = 1.7 \times 10^{-10}$ C/m. However, a more realistic estimation based upon the simulation in Fig. 1 shows that for $Q_l = 1 \times 10^{-10}$ C/m the diffusion wing already reaches the quadrupole rods. Thus, one may expect reduced ion capacity for ion species having a long diffusion wing.

Fig. 2 shows the ion number density distributions having various diffusion spreads. The results of two separate simulations are shown in each figure, one for singly charged ions $m = 1000$ and the other for $+17$ ions having $m = 17{,}000$. Fig. 2a shows the case of a relatively weak RF focusing, $V_{RF} = 30$ V. The diffusion spread estimated using Eq. (15) is $\Delta r \approx 2.1$ mm for singly charged ions and $\Delta r \approx 0.5$ mm for $+17$ ions. These estimates agree well with the diffusion spreads seen in Fig. 2a.

The maximum charge capacity (13) for the conditions in Fig. 2a is $Q_{max} = 4.2 \times 10^{-11}$ C/m, four times larger then the value used for the simulations. However, due to the extended diffusion wing we may expect that the singly charged ions in Fig. 2a approach the maximum capacity limit at a lower value of $Q_l = 10^{-11}$ C/m.

Fig. 2b shows density distributions for the case of increased RF voltage, $V_{RF} = 150$ V. Because of the increased charge capacity, we have specified an increased linear charge density in order to have the ion cloud radius comparable to the one in Fig. 2a. Now the diffusion spread (15) gives 0.41 and 0.1 mm, correspondingly. The diffusion spread is small compared to the radial size of the ion cloud, and the charge capacity approaches the zero-temperature limit (13) for each of the ion species considered.

The results in Fig. 2 were obtained for the bath gas pressure of 10 mTorr. At this pressure the mean-free path for the ion–neutral collisions is smaller than the quadrupole radial dimension ρ. The theoretical relationships (11–17) do not take into account the bath gas pressure. Thus, it is of interest to model the ion density distribution for various pressure conditions. Fig. 3 shows the ion density distribution simulated for the bath gas pressure of 0.1 mTorr, i.e., two orders of magnitude lower pressure compared to one used in Figs. 1 and 2. The free path becomes larger than the characteristic radial size ρ, so one may expect the ion density distribution to be different from the higher pressure one. For comparison the 10 mTorr distributions for ions $m = 1000$ (+1) and $m = 17{,}000$ (+17) are also

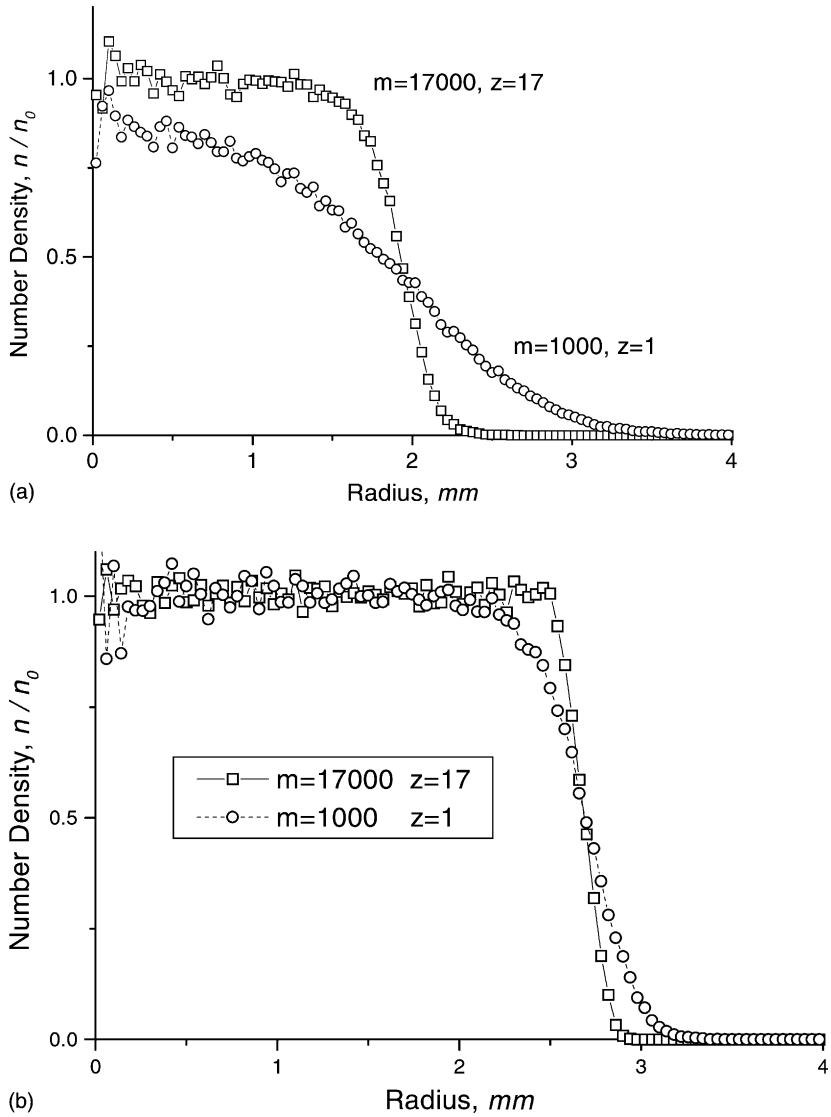

Fig. 2. Diffusion spread of the ion density distribution. The ion cloud consists of a single ion species having $m/z = 1000$. Singly charged ions ($m = 1000$) and +17 ions ($m = 17{,}000$) are considered, with ion–neutral collision cross-section 200 and 3400 A^2, respectively. (a) 1×10^{-11} C/m, $V_{RF} = 30$ V, frequency 600 kHz, $q_m = 0.05$, pressure 10 mTorr, and $R_q = 1.95$ mm. (b) 4.8×10^{-10} C/m, $V_{RF} = 150$ V, frequency 600 kHz, $q_m = 0.25$, pressure 10 mTorr, and $R_q = 2.7$ mm.

shown. Instead of the number density, here we show the radial density $2\pi rn(r)$, in order to emphasize the behavior at larger radii. One can see that the diffusion spread for the lower pressure becomes slightly shorter. However, the pressure-dependent difference is not as significant as the dependence on the ion charge.

The time needed for the ion density distribution to reach equilibrium at the 0.1 mTorr pressure is $\gtrsim$10 ms. The results shown in Fig. 3 are based on the statistics collected for simulation times >25 ms. The time step dt for the ion trajectory tracing must be much smaller than the RF period; d$t \approx 20$ ns has been used. Thus,

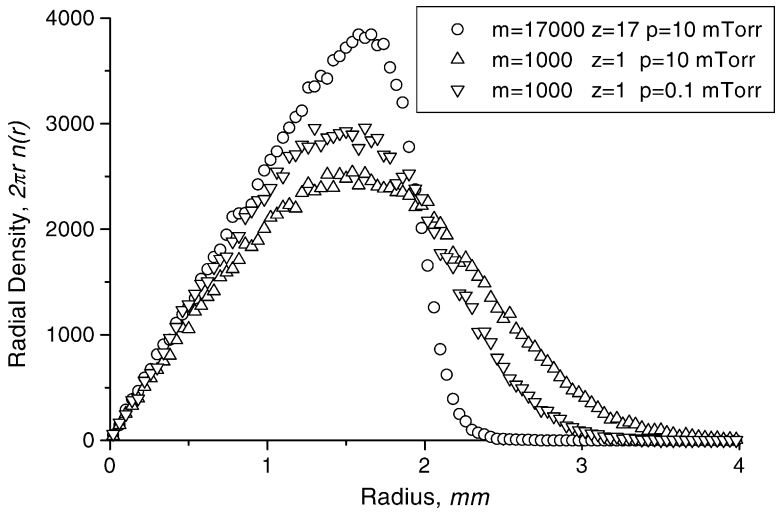

Fig. 3. The diffusion spread for pressure 10 and 0.1 mTorr for singly charged ions ($m = 1000$). The radial ion density distribution is shown. For comparison the results for +17 ions ($m = 17{,}000$) for 10 mTorr are shown (circles). The linear charge density is 1×10^{-11} C/m ($R_q = 1.95$ mm), $V_{RF} = 30$ V, frequency 600 kHz, and $q_m = 0.05$.

the simulation for 0.1 mTorr pressure required a long computation time, ~2 days. It takes additional analysis of the possible computation errors to arrive at quantitative results for this pressure range. The conclusion that can be reached based on the results in Fig. 3 is that the approximate relationships can still be roughly applicable down to pressures of ~0.1 mTorr.

These results for the diffusion spread allow one to predict conditions for preferential accumulation of highly charged ions having a high-molecular mass. This should take place under a reduced RF potential, when smaller ion species can escape radially through the diffusion wing. One more necessary condition is that the ion current must be small, so that the time of filling the quadrupole is much longer than the collisional relaxation time τ (9), to ensure a sufficient collisional relaxation of ions. This external accumulation mode can be of interest when the sensitivity for large ion species needs to be increased, for example, for measurements for intact proteins. Note that this approach differs from the usual low-mass cut-off in RF quadrupoles, when low m/z ions have q-parameters above the stability limit (2). Here, instead of increasing q_m, we suggest using a reduced RF voltage V_{RF}. External accumulation is thus obtained using a low-input current and long accumulation time conditions, to provide preferential accumulation of species having a shorter diffusion spread. Thus, it should be possible to distinguish between ions having similar m/z values, but different masses.

We now move our attention to a more complicated case of an ion cloud consisting of several m/z ion species. It has been reported that the space charge can force the ions of different m/z to occupy different radial positions inside the collisional RF multipole. The phenomenon was observed in computer simulations and confirmed experimentally for collisional RF quadrupoles used both for the external accumulation and as ion guides [29]. The theoretical treatment has also been reported in Refs. [29,30]. The accurate two-dimensional computer model used in the present study has allowed us to obtain additional details on the ion stratification phenomenon.

The simulations were performed in the same way as described earlier, but this time the ion cloud consisted of three ion species, having $m = 6000$ and charge states +4, +5, and +6. The RF quadrupole parameters are as follows: inscribed radius $\rho = 4$ mm,

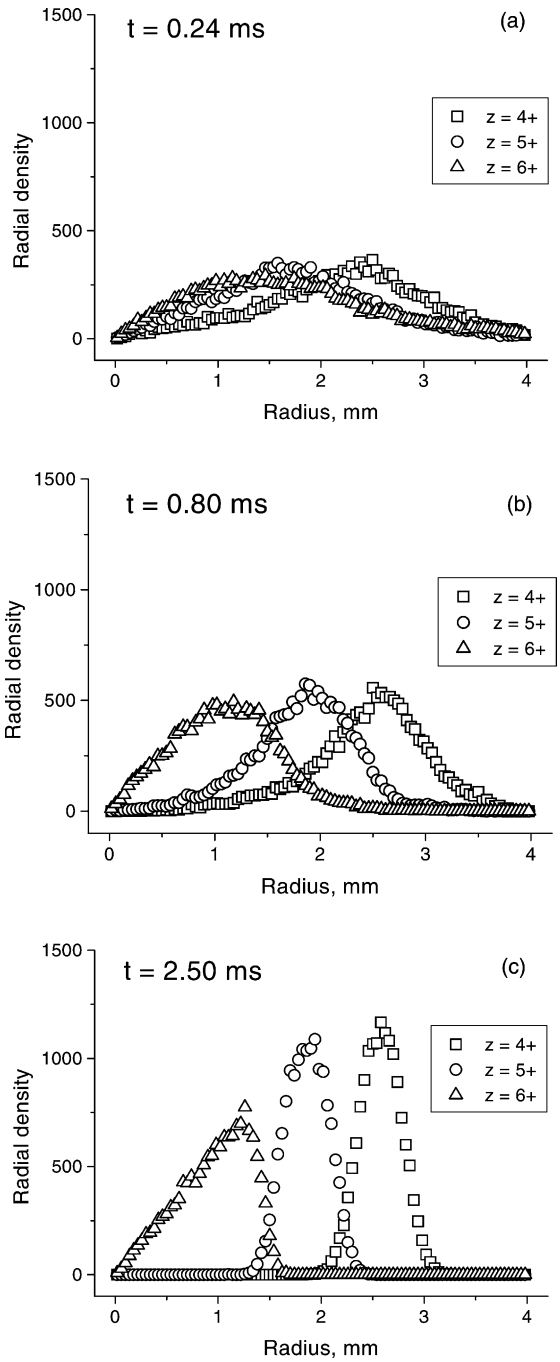

Fig. 4. Radial ion density distribution for an ion cloud consisting of three charge states $z = +4$, $+5$, and $+6$ of ions ($m = 6000$) for bath gas pressure of 10^{-3} Torr. The evolution is shown for cooling times (a) $t = 0.24$ ms, (b) $t = 0.80$ ms, and (c) $t = 2.5$ ms. At $t = 0$ ions having thermal kinetic energy were distributed

$V_{RF} = 100$ V, and frequency 600 kHz. This system roughly corresponds to the experimental study on the external accumulation of insulin ions reported previously [29]. The collision cross-section used for the simulations, $\sigma = 1200\,A^2$, was estimated using interpolation of experimental cross-section values measured by others for protein ions [34,35].

Fig. 4 shows the radial ion density distribution as it evolves with the cooling time t. Initial conditions were specified as follows: the thermal kinetic energy ions were distributed uniformly over a cylinder of 4.2 mm diameter. The buffer gas was assumed to have molecular mass $m_g = 29$ (i.e., the weighted average of the N_2 and O_2 molecular masses) and a number density corresponding to 1 mTorr pressure. The collisional relaxation time for the ion velocity, estimated for these parameters using Eq. (9), is $\tau = 0.8$ ms. The radial density was calculated as the number of macro-ions per 0.04 mm radial bin. To have sufficient statistics, this calculation was repeated 100 times over a short time interval. Fig. 4a and b show the radial ion density distribution for $t = 0.3\tau = 0.24$ ms, and $t = \tau = 0.8$ ms when the relaxation of ions is still under way. After the relaxation time $t \gtrsim \tau$ the radial density takes an equilibrium shape shown in Fig. 4c. This stationary distribution can be compared with one derived theoretically [29,30] based on assumptions of a high-space charge and low-ion kinetic energy. The approximation results in a constant ion number density n_0, same as defined by Eq. (11). Each ion species, i, must be located in a separate cylindrical layer, from R_{0i} to R_{1i}, so that the total charge per the quadrupole length is equal to the stored linear charge Q_i for the

distributed uniformly over a cylinder of 4.2 mm o.d. The number of super-ions used for the simulation is 450 (150 for each charge state) per 4 mm of the quadrupole's length; the charge of each super-ion corresponds to 416 ion charges. The linear charge density is 4×10^{-11}, 5×10^{-11}, and 6×10^{-11} C/m for each charge state correspondingly. The RF quadrupole parameters are as follows: $\rho = 4$ mm, $V_{RF} = 100$ V, frequency 600 kHz, $q_m = 0.11$, $q_m = 0.14$, and $q_m = 0.17$ correspondingly. The radial borders of the stratified ion structure estimated under the low-ion energy approximation [29,30] are 0–1.432 mm for +6 ions, 1.568–2.124 mm for +5 ions, and 2.374–2.772 mm for +4 ions.

i-th ion species:

$$Q_i = \pi(R_{1i}^2 - R_{0i}^2)ez_i n_0 \quad (18)$$

Here z_i is the charge state of the *i*-th ion species. An additional equation for the unknown radii R_{0i}, R_{1i} can be obtained from the balance of the space charge field and effective RF focusing field [20,30]. The radial positions estimated using this approach are listed in the caption for Fig. 4. One can see that the simulated equilibrium distribution in Fig. 4c possesses radial positions close to the estimated values. The radial density $2\pi rn(r)$ for the +6 and +5 charge states increases proportionally with the radius *r*, which agrees with the expected constant ion number density, $n(r) = n_0$. The borders of each layer are diffused, similar to ion density distributions for single *m*/*z* ion clouds considered earlier. This radial spread accounts for the observed reduced ion number density for +6 ions.

Summarizing results in Fig. 4, we conclude that the stratified ion density distribution establishes itself upon the completion of the collisional relaxation. The number density and radial positions of the simulated equilibrium distribution agree well with theoretical estimates.

The direct computer model used in our study is capable of realistic simulation of the ion kinetic energy evolution. There is no established formalism describing the collisional cooling dynamics. The drag coefficient approaches reviewed in Ref. [35] do not account for the discrete nature of collisions and other realistic details, such as the combination of the collisional cooling in the axial direction and radial excitation of ions by the intense multipolar RF electric field.

The simulation results for the collisional cooling dynamics for the bath gas pressure 1 mTorr are presented in Figs. 5 and 6. The initial ion kinetic energy is $E_z = 10$ eV per elementary charge, with the initial velocity vector directed along the quadrupole axis. All other parameters for the ion cloud and for the RF quadrupole are the same as used for the simulations in Fig. 4. It is expected from the theoretical study [18] that the ion velocity will be damped by collisions, with the characteristic exponential time constant τ, Eq. (9), until thermal equilibrium is established. To verify this assumption we have plotted the ion kinetic energy in the units of thermal energy per one degree of freedom, $E_{kt} = kT/2 \approx 1/80$ eV. It is seen from the logarithmic plot $E_z(t)$ in Fig. 5 that the ion kinetic energy is reduced 10 times each ~1 ms. The

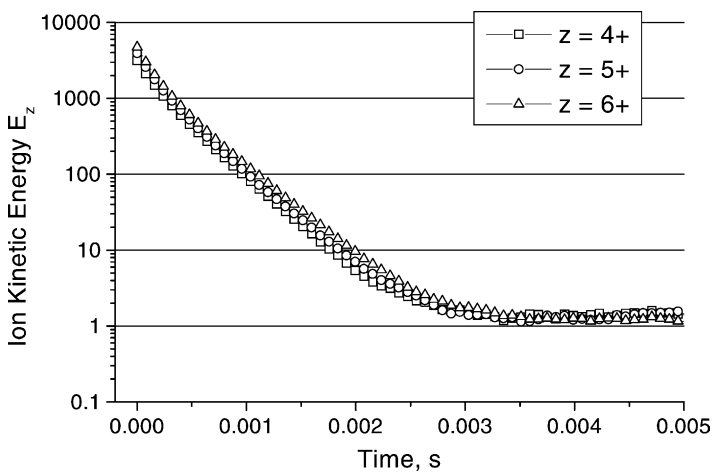

Fig. 5. The collisional relaxation of the ion kinetic energy for a bath gas pressure 10^{-3} Torr. The initial ion velocity is directed along the quadrupole axis and corresponds to 10 eV per elementary charge. The axial component E_z is plotted in units of the thermal energy $E_{kt} = 0.5kT \approx 1/80$ eV. The RF quadrupole parameters are same as for Fig. 4. The simulation involves 900 macro-ions, each carrying 208 ion charges.

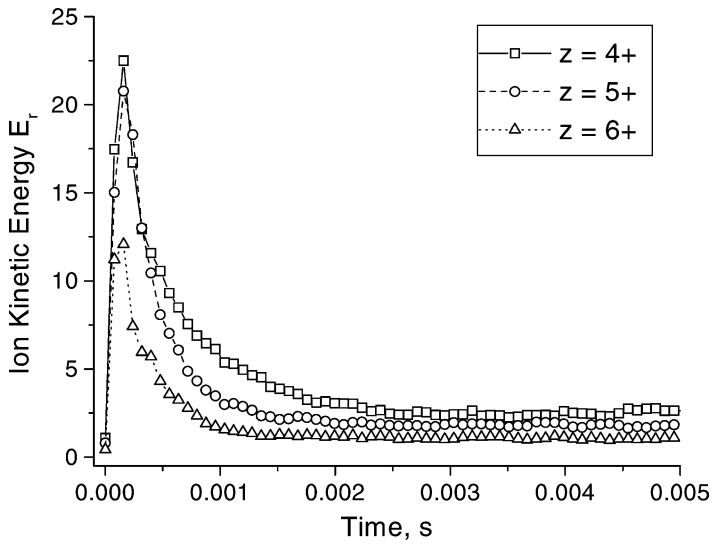

Fig. 6. The evolution of the radial component of the ion kinetic energy E_r. Same conditions as in Fig. 4 are used; E_r is expressed in units of the thermal energy $E_{kt} = 0.5kT \approx 1/80$ eV.

characteristic time estimated using Eq. (9) for conditions of the simulation is $\tau \approx 0.8$ ms, meaning that the kinetic energy must be reduced 10 times over the time interval of $0.5\tau \ln 10 \sim 1$ ms. In fact for higher ion kinetic energies the rate of collisional cooling must increase [18,35]. Such a trend can be observed in Fig. 5. After 3 ms of the collisional relaxation the axial component of the kinetic energy reaches a stationary level, just slightly above the expected thermal energy value. We can conclude that both the rate of collisional cooling and the equilibrium energy level agree with the estimations based on the collisional cooling mechanism. (Note that in our two-dimensional model we disregard the axial electric fields arising from the ion–ion interaction, because each ion is replaced by an infinite charged cylinder when the space charge interactions are calculated. Thus, the contribution of the ion–ion interaction to kinetic energy relaxation applies here only for the radial ion kinetic energy.)

Fig. 6 shows the radial component of the average ion kinetic energy, obtained in the same simulation as in Fig. 5. This time there is no theory available to treat the simulation results. Transformation of the axial energy component into the radial one is of great practical interest, because it may define efficiency of the RF quadrupole collisional cells or two-dimensional ion traps. It is often assumed that the stationary kinetic energy approaches the thermal level, however, it is difficult to estimate theoretically how the RF ion motion will influence the thermal equilibrium. In order to distinguish between the energy of RF oscillations and the random energy of the ion motion, we have used the instantaneous ion velocities taken for the RF phase corresponding to zero energy of the RF oscillations. Thus, the radial kinetic energy E_r considered here excludes the energy of RF oscillations, and can be regarded as the energy of an averaged, or secular ion motion [33]. We also use the term "random energy" because it is randomly distributed over the XY coordinate plane, as a result of relaxation. The same units of thermal energy are used as in Fig. 5. The radial energy E_r is calculated as a sum of two energy components E_x and E_y, so the thermal level would be $E_r = 2E_{kt}$. The simulation has resulted in the following stationary radial kinetic energy levels: $2.6E_{kt}$ for $+4$ ions, $1.9E_{kt}$ for $+5$ ions, and $1.1E_{kt}$ for $+6$ ions. Higher than thermal energy for $+4$ ions can be explained by a higher intensity of RF excitation, due to

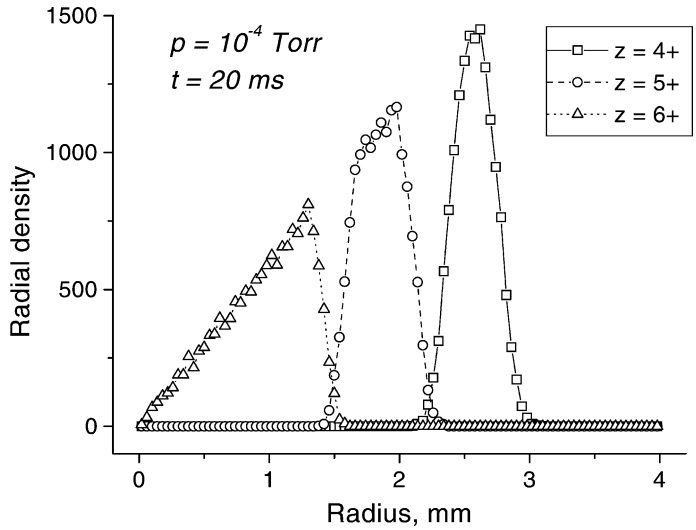

Fig. 7. The equilibrium radial ion density distribution for a bath gas pressure 10^{-4} Torr. All other parameters are same as in Fig. 4.

higher radial positions for these ions, see Fig. 4c. Energy levels lower than the expected $2E_{kt}$, as observed for +6 ions, were unexpected. A possible explanation is presented as follows.

Simulations showed that the sub-thermal ion energy is observed for low-pressure conditions. Fig. 7 shows the equilibrium radial ion density distribution for the bath gas pressure 10^{-4} Torr. All other parameters are same as in Fig. 4. The diffusion spread is reduced relative to the higher pressure case in Fig. 4c, which can be seen in the slightly reduced overlap of the distribution peaks. Note that the free path before collisions is ∼1 cm, one order of magnitude larger than for the 1 mTorr pressure simulation, in apparent contradiction with sharp radial borders seen in Fig. 7. We have arrived at the conclusion that the sharper radial structure is due to the lower random kinetic energy of ions observed at lower pressures, as confirmed by the following results.

Figs. 8 and 9 show the average ion kinetic energy evolution, simulated for 0.1 mTorr bath gas pressure. The initial kinetic energy of ions is $E_z = 1$ eV per elementary charge; all other parameters are same as for Figs. 5 and 6. The characteristic time for 10 times decrease of the axial kinetic energy is ∼10 ms, consistent with the pressure-dependent collisional relaxation time τ, Eq. (9). The equilibrium energy approaches the expected thermal level, $E_z \sim E_{kt}$ for $t > 20$ ms. The radial kinetic energy shows a different cooling rate, reaching stationary levels in ∼10 ms; +6 ions reach a stationary level in a shorter time than +5 and +4 ions. The simulation has resulted in the following stationary radial kinetic energy levels: $0.6E_{kt}$ for +4 ions, $0.4E_{kt}$ for +5 ions, and $0.2E_{kt}$ for +6 ions. All three ion species have arrived at random radial kinetic energy levels considerably lower than the expected thermal equilibrium level $2E_{kt}$. A possible explanation for the sub-thermal radial energies is ion–ion cooling: all ions are incorporated into the space charge defined structure, and an excess energy of each ion becomes eventually distributed over the whole ion ensemble. The stationary random ion kinetic energy is defined by equilibrium between the excitation from ion–neutral collisions and the ion–ion relaxation. At lower pressures, $\sim 10^{-4}$ Torr, the ion–neutral collision rate is decreased and the equilibrium shifts to the sub-thermal level. In other words, in the low-pressure limit the thermal equilibrium ion velocity is defined by the effective mass that approaches the total mass of the whole ion ensemble.

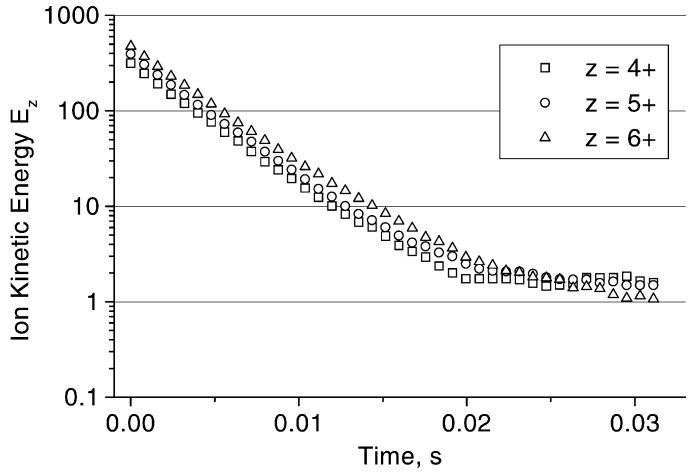

Fig. 8. The collisional relaxation of the ion kinetic energy for a bath gas pressure 10^{-4} Torr. The initial ion velocity is directed along the quadrupole axis and corresponds to 1 eV per elementary charge. The axial component E_z is plotted in units of the thermal energy $E_{kt} = 0.5kT \approx 1/80$ eV. All other parameters are same as for Fig. 4.

It must be emphasized that the lower-than-thermal energies are obtained for the random part of the radial component of the ion kinetic energy, which does not include the kinetic energy of RF oscillations of ions, W_{RF}. The latter value is equal by definition to the pseudo-potential of the RF multipolar field at the ion's radial position [33]. For the higher ion populations the ion cloud extends to the higher radii, and the kinetic energy of RF oscillations increases. For example, for +4 ions oscillating around 2.7 mm radial position, for parameters in Fig. 4, $W_{RF} \sim 20$ eV per elementary charge. This results in an ion–neutral collision energy the same as if 20 eV_{lab} ions are injected into the collisional cell. The high energy of collisions results in ion fragmentation, called "multipole storage assisted dissociation" (MSAD) [7–10,40]. The ion population corresponding to the onset of MSAD has been theoretically estimated in [20]. Thus, lower-than-thermal

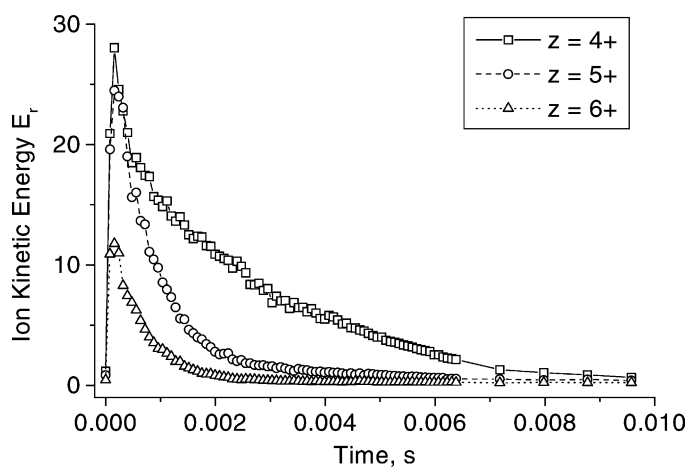

Fig. 9. Evolution of the radial component of the ion kinetic energy E_r obtained from the same simulation as in Fig. 8. E_r is expressed in units of the thermal energy $E_{kt} = 0.5kT \approx 1/80$ eV.

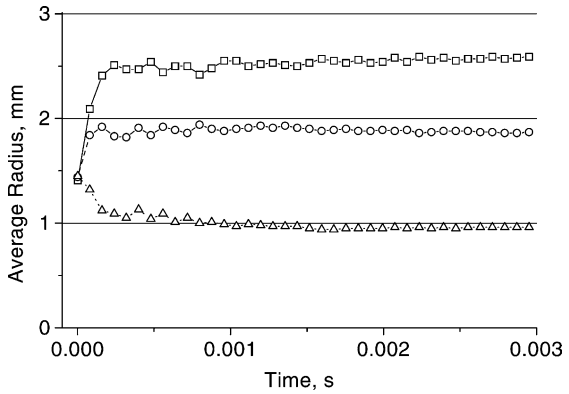

Fig. 10. The average radius of ions +4 (squares), +5 (circles), and +6 (triangles) obtained from the same simulation as in Figs. 8 and 9.

random energies discussed earlier can be accompanied by quite high-collision energies and consequently high internal ion energies.

Fig. 10 shows an average radial position vs. cooling time, calculated for each of the three ion species considered, for 1 eV initial ion energy and 10^{-4} Torr pressure, i.e., same conditions as for Figs. 8 and 9. The average radius arrives at the stationary level in ~1 ms, much faster than it takes for the energy relaxation. This observation may be of interest for experimental conditions, when externally accumulated ions do not have sufficient time for complete collisional relaxation, e.g., due to a low-bath gas pressure. It follows that reduced accumulation efficiency for higher m/z ions may be expected under such conditions, although not as distinct as for fully relaxed ions.

To verify the assumption, that the space charge interactions are responsible for sub-thermal secular ion kinetic energy, we have performed simulations for the same conditions as in Figs. 8 and 9, but with zero linear charge density. This was done by specifying a zero charge for each macro-ion for the ion–ion interaction calculations. The resulting radial ion density distribution is shown in Fig. 11. The simulation results for different charge states are shown using the same symbols as in previous figures. The corresponding curves show the theoretical radial ion density distributions expected for the case of a negligible space charge [18,19]:

$$2\pi r n(r) = N_l \frac{2r}{R_{kT}^2} \exp\left(-\frac{r^2}{R_{kT}^2}\right) \tag{19}$$

The characteristic radial size R_{kT} is defined by Eq. (17). Integration of the distribution Eq. (19) over radius gives the number of ions per unit length of the quadrupole N_l. The relationship (19) represents

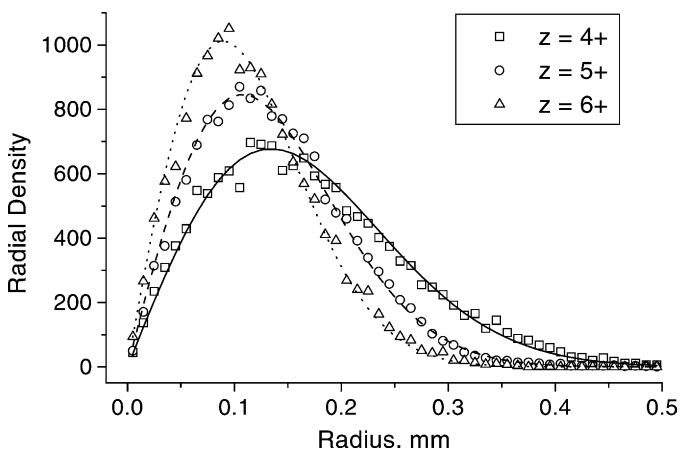

Fig. 11. The equilibrium radial ion density distribution for a zero space charge conditions. Simulation results (symbols) are plotted together with the theoretical low-charge ion density distributions, calculated for each charge state using Eq. (19). The characteristic radial width R_{kT} is calculated using Eq. (17): 0.190 mm for +4 ions, 0.152 mm for +5 ions, and 0.127 mm for +6 ions. The simulation uses 450 super-ions (150 for each charge state); the charge of each super-ion is set to 0 to cancel the ion–ion interaction. The bath gas pressure 10^{-4} Torr. All other parameters are same as in Figs. 4 and 7.

the Boltzmann distribution for thermal particles in a potential well created by the pseudo-potential of the RF quadrupole electric field [18]. Note that there are no adjustable parameters in (19), and the theoretical curves are plotted in Fig. 11 exactly as defined by Eqs. (17) and (19). The good agreement between the theoretical distributions and simulated distributions for each charge state in Fig. 11 shows that under zero space charge conditions ions arrive at thermal equilibrium with the bath gas. The average kinetic energy of the secular ion motion produced by this simulation is $E_r = (2 \pm 0.2)E_{kT}$ and $E_z = (1 \pm 0.2)E_{kT}$, corresponding to the thermal energy E_{kT} per each degree of freedom. The results support the assumption that the ion space charge gives a significant contribution to the ion radial kinetic energy relaxation under the low-pressure conditions.

The infinite two-dimensional space charge elements used in our model allow for accurate modeling of radial ion–ion interactions, but disregard the axial ion–ion interactions. We have used an alternative three-dimensional model (see Section 2) to estimate the space charge influence on the ion kinetic energy relaxation in the axial direction. Preliminary results have confirmed that the ion–ion interaction results in a faster ion kinetic energy relaxation at pressures ~0.1 mTorr, for both radial and axial components of ion kinetic energy. Quantitative results using the three-dimensional approach will require a computation power at least one order of magnitude greater than in the present study (which used a 1 GHz processor PC).

All results shown so far were obtained for an RF quadrupole. The computer model used can also simulate RF multipoles of any order. These observations can be generalized for higher order multipoles, if corresponding theoretical relationships are used [18–20,30]. As an example, we show the radial ion density distribution simulated for an RF octopole, Fig. 12. The collisional relaxation time estimated

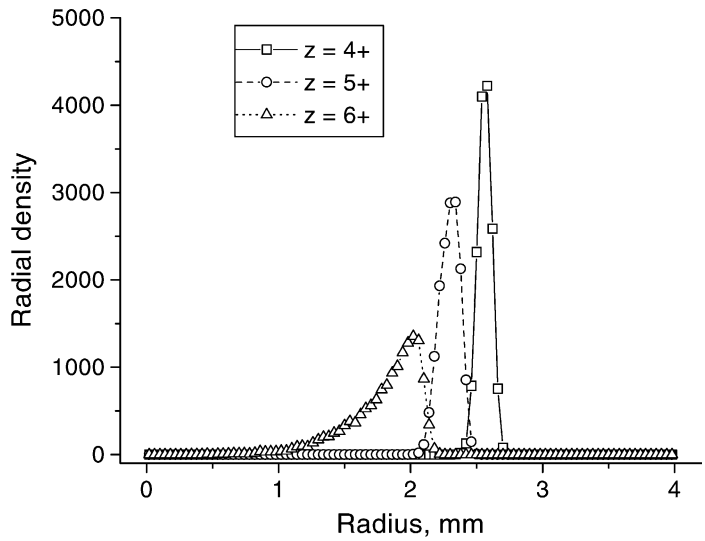

Fig. 12. The equilibrium radial ion density distribution for the RF octopole. The ion cloud consists of $m = 6000$ ions having three charge states $z = +4$, $+5$, and $+6$. The bath gas pressure 4×10^{-4} Torr. At $t = 0$ ions having thermal kinetic energy were distributed uniformly over a cylinder of 4.2 mm o.d. The collisional cooling time $t = 4$ ms. The number of super-ions used for the simulation is 450 (150 for each charge state) per 4 mm axial interval; the charge of each super-ion corresponds to 832 ion charges. The linear charge density is 8×10^{-11}, 1×10^{-10}, and 1.2×10^{-10} C/m for each charge state correspondingly. The RF octopole parameters are as follows: inscribed radius $\rho = 4$ mm, $V_{RF} = 500\,V_{0-p}$, frequency 3000 kHz, stability parameters [30] $q_{N1} = 0.202$ (+6 ions), $q_{N2} = 0.168$ (+5 ions), and $q_{N3} = 0.135$ (+4 ions). The radial borders of the stratified ion structure estimated under the low-ion energy approximation [30] are 0–2.107 mm for +6 ions, 2.172–2.403 mm for +5 ions, and 2.494–2.626 mm for +4 ions.

for parameters in Fig. 12 is $\tau = 2$ ms. The simulation has shown an established stationary ion density distribution for $t > 4$ ms, in agreement with the expected completion of collisional relaxation. A distinct stratified structure is produced, with radial positions consistent with theoretical values, listed in the caption for Fig. 12.

4. Conclusions

A computer model based on the direct calculation of ion trajectories in RF multipole electric fields, together with realistic simulations of ion–neutral and ion–ion interactions, has allowed us to study details of the ion cloud relaxation dynamics and the equilibrium ion cloud shape in two-dimensional RF multipole ion traps. Simulations have confirmed that with increasing the stored ion population the radial size of the ion cloud increases. The equilibrium distribution parameters, such as ion number density, radial size, and diffusion spread of the radial border, were found to be consistent with theoretical estimates. We conclude that the simulations confirm theoretical relationships for the two-dimensional RF multipole ion trap ion capacity [20]. Taking into account the diffusion "wing" of the distribution results in a somewhat higher capacity for same m/z ions with higher ion charge (i.e., higher mass).

In the case of an ion cloud consisting of several m/z ion species, simulated using three charge states of $m = 6000$ ions, the simulations have confirmed that ions of different m/z occupy on average different radial positions, with higher m/z ions occupying higher radii. This stratified structure becomes more distinct for higher stored ion populations, and for reduced bath gas pressures. The diffusional spread of the radial borders decreases with increasing mass, resulting in more distinct stratification for multiply charged ions, compared to singly charged ions that have same m/z values. An additional smearing of the borders arises due to ion RF oscillations, $\Delta r_{RF} = q_m r$ [30], where q_m is q-parameter, Eq. (2), and r is the radial position. In all cases considered here $q_m \ll 0.91$, so that ions are far from instability. Thus Δr_{RF} is small, $\ll r$. The space charge influence on the ion stability is not confirmed by simulations for low q_m conditions. In contrast, lower m/z ions drift to smaller radial positions, with characteristic times much shorter than the collisional relaxation time (Fig. 10).

The model presented uses the classical hard spheres approach for ion–neutral collisions. Although idealized, the approach allows one to observe details of the ion collisional relaxation process in the context of the standard model. The ion relaxation dynamics are followed for realistic conditions that include RF-driven ion motion and ion–ion interactions. Conversion of the kinetic energy between secular axial and radial components and the kinetic energy of RF oscillations is observed. We have estimated characteristic times for establishing the stratified structure of the ion density distribution and for relaxation of axial and radial components of the ion secular kinetic energy. The ion energy relaxation for zero space charge conditions proceeds with a characteristic time given by collisional relaxation theory. Faster relaxation rates are observed for conditions of frequent ion–ion interactions. Simulations indicate that ion–ion cooling can result in the faster relaxation and lower than thermal values of the random radial kinetic energy at low-bath gas pressures and high ion populations. As a result, the radial layers of different m/z ions acquire a sharper, more distinct structure under such conditions.

The detailed description of the ion density distribution obtained allows one to derive basic conditions for efficient, non-discriminative ion accumulation and storage. Conditions causing full relaxation of the ion kinetic energy are important, particularly for its radial component (which defines the radial spread of the ion density distribution). This can be achieved using a sufficiently high buffer gas pressure and small initial ion kinetic energy. The axial DC potential well depth should be small enough to minimize the initial ion kinetic energy, yet still sufficient for trapping sufficient ion charge, as estimated in Ref. [20]. Experimental results [7,14,41] indicate that the DC offset between the accumulation multipole and orifices at its ends influences observed ion fragmentation and

mass-discrimination phenomena. It is interesting to note that the amount of charge trapped in the RF multipole can be much greater than the ion population needed for FT ICR mass analysis, e.g., 10^9 elementary charges per meter for Figs. 4–10. These high-ion populations result in a significant alteration of the ion-optical properties of the RF multipole, leading to additional mass-discrimination effects, not only for the ion cloud in equilibrium, but also for ion trapping, relaxation, and subsequent extraction processes. One can assume that existing experimental observations for the high accumulated ion populations also exhibit a combination of mass-discrimination effects resulting from ion accumulation, extraction, transport to the mass analyzer, and the mass analysis itself. Experiments have shown that restricting the accumulated ion population to below a certain limit can reduce mass discrimination, e.g., when using reduced axial DC trapping voltages [41]. In the recently described DREAMS approach [17], the ion population is controlled in a data-dependent fashion, which prevents the accumulation quadrupole from overfilling and results in further improvement in sensitivity and dynamic range.

Acknowledgements

We thank Drs. K. Tang and C.D. Masselon for helpful discussions. Portions of this research were supported by the US Department of Energy, Office of Biological and Environmental Research, and the National Center for Research Resources under Grant RR12365. The Pacific Northwest National Laboratory is operated by Battelle Memorial Institute for the US Department of Energy through contract DE-AC06-76RLO 1830.

References

[1] D.J. Douglas, J.B. French, J. Am. Soc. Mass Spectrom. 3 (1992) 398.
[2] H.J. Xu, M. Wada, J. Tanaka, H. Kawakami, I. Katayama, Nucl. Instrum. Methods Phys. Res. A 333 (1993) 274.
[3] A.N. Krutchinsky, I.V. Chernushevich, V.L. Spicer, W. Ens, K.G. Standing, J. Am. Soc. Mass Spectrom. 9 (1998) 569.
[4] H.G. Dehmelt, Adv. Atom. Mol. Phys. 3 (1967) 53.
[5] M.W. Senko, C.L. Hendrickson, M.R. Emmett, S.D. Shi, A.G. Marshall, J. Am. Soc. Mass Spectrom. 8 (1997) 970.
[6] J.M. Campbell, B.A. Collings, D.J. Douglas, Rapid Commun. Mass Spectrom. 12 (1998) 1463.
[7] K. Sannes-Lowery, R.H. Griffey, G.H. Kruppa, J.P. Speir, S.A. Hofstadler, Rapid Commun. Mass Spectrom. 12 (1998) 1957.
[8] S.A. Hofstadler, K.A. Sannes-Lowery, R.H. Griffey, Rapid Commun. Mass Spectrom. 13 (1999) 1971.
[9] S.A. Hofstadler, K.A. Sannes-Lowery, R.H. Griffey, Anal. Chem. 71 (1999) 2067.
[10] K.A. Sannes-Lowery, S.A. Hofstadler, J. Am. Soc. Mass Spectrom. 11 (2000) 1.
[11] B. Cha, M. Blades, D.J. Douglas, Anal. Chem. 72 (2000) 5647.
[12] M. Welling, H.A. Schuessler, R.I. Thompson, H. Walther, Int. J. Mass Spectrom. Ion Processes 172 (1998) 95.
[13] M. Belov, E. Nikolaev, G.A. Anderson, H.R. Udseth, T.P. Conrads, T.D. Veenstra, C.D. Masselon, M.V. Gorshkov, R.D. Smith, Anal. Chem. 73 (2001) 253.
[14] M.E. Belov, E.N. Nikolaev, R. Harkewicz, C.D. Masselon, K. Alving, R.D. Smith, Int. J. Mass Spectrom. 208 (2001) 205.
[15] M.E. Belov, E.N. Nikolaev, G.A. Anderson, K.J. Auberry, R. Harkewicz, R.D. Smith, J. Am. Soc. Mass Spectrom. 12 (2001) 38.
[16] R. Harkewicz, M.E. Belov, G.A. Anderson, L. Paša-Tolic, C.D. Masselon, D.C. Prior, H.R. Udseth, R.D. Smith, J. Am. Soc. Mass Spectrom. 13 (2002) 144.
[17] M.E. Belov, G.A. Anderson, N.H. Angell, Y. Shen, N. Tolic, H.R. Udseth, R.D. Smith, Anal. Chem. 73 (2001) 5052.
[18] A.V. Tolmachev, I.V. Chernushevich, A.F. Dodonov, K.G. Standing, Nucl. Instrum. Methods Phys. Res. B 124 (1997) 112.
[19] G.-Z. Li, J.A. Jarrell, in: Proceedings of the 45th ASMS Conference on Mass Spectrometry and Allied Topics, Orlando, FL, 1998, p. 491.
[20] A.V. Tolmachev, H.R. Udseth, R.D. Smith, Anal. Chem. 72 (2000) 970.
[21] C.M. Lock, E.W. Dyer, Rapid Commun. Mass Spectrom. 13 (1999) 422.
[22] F.A. Londry, R.L. Alfred, R.E. March, J. Am. Soc. Mass Spectrom. 4 (1993) 687.
[23] R.K. Julian, M. Nappi, C. Weil, R.G. Cooks, J. Am. Soc. Mass Spectrom. 6 (1995) 57.
[24] R.G. Cooks, C.D. Cleven, L.A. Horn, M. Nappi, C. Weil, M.H. Soni, R.K. Julian Jr, Int. J. Mass Spectrom. Ion Processes 146/147 (1995) 147.
[25] M. Nappi, C. Weil, C.D. Cleven, L.A. Horn, H. Wollnik, R.G. Cooks, Int. J. Mass Spectrom. Ion Processes 161 (1997) 77.
[26] D.W. Mitchell, R.D. Smith, Int. J. Mass Spectrom. Ion Processes 165/166 (1997) 271.
[27] D.W. Mitchell, J. Am. Soc. Mass Spectrom. 10 (1999) 136.
[28] M.A.N. Razvi, X.Z. Chu, R. Alheit, G. Werth, R. Blumel, Phys. Rev. A 58 (1998) R34.
[29] A.Tolmachev, R. Harkewicz, C. Masselon, G. Anderson, V. Rakov, L. Pasa-Tolic, E. Nikolaev, M. Belov, H. Udseth, R. D. Smith, in: Proceedings of the 48th ASMS Conference, Long Beach, CA, June 2000, p. 115 (CD ROM).

[30] A.V. Tolmachev, H.R. Udseth, R.D. Smith, Rapid Commun. Mass Spectrom. 14 (2000) 1907.
[31] P.H. Dawson (Ed.), Quadrupole Mass Spectrometry and Its Applications, North-Holland, Amsterdam, 1976, pp. 20, 80.
[32] D.A. Dahl, SIMION 3D Version 6.0, Users' Manual Publication No. INEL-95/0403, Lockheed Idaho Technologies Company, Idaho Falls, ID, USA, 1995.
[33] D. Gerlich, in: C.Y. Ng, M. Baer (Eds.), State Selected and State-to State Ion-Molecule Reaction Dynamics. Part 1. Experiment, vol. LXXXII, Wiley, New York, 1992, p. 1.
[34] T. Covey, D.J. Douglas, J. Am. Soc. Mass Spectrom. 4 (1993) 616.
[35] Y.-L. Chen, B.A. Collings, D.J. Douglas, J. Am. Soc. Mass Spectrom. 8 (1997) 681.
[36] D.J. Douglas, J. Am. Soc. Mass Spectrom. 9 (1998) 101.
[37] I.M. Sobol, The Monte-Carlo Method, The University of Chicago Press, Chicago, 1974.
[38] E.W. McDaniel, E.A. Mason, The Mobility and Diffusion of Ions in Gases, Willey-Interscience, New York, 1973.
[39] A. Dodonov, V. Kozlovskiy, A. Loboda, V. Raznikov, I. Sulimenkov, A. Tolmachev, H. Wollnik, A. Kraft, Rapid Commun. Mass Spectrom. 11 (1997) 1649.
[40] K. Hakansson, J. Axelsson, M. Palmblad, P. Håkansson, J. Am. Soc. Mass Spectrom. 11 (2000) 210.
[41] K. Alving, M.E. Belov, A.V. Tolmachev, L. Paša-Tolic, R.D. Smith, in: Proceedings of the 49th ASMS Conference on Mass Spectrometry and Allied Topics, Chicago, IL, May 2001 (CD ROM).